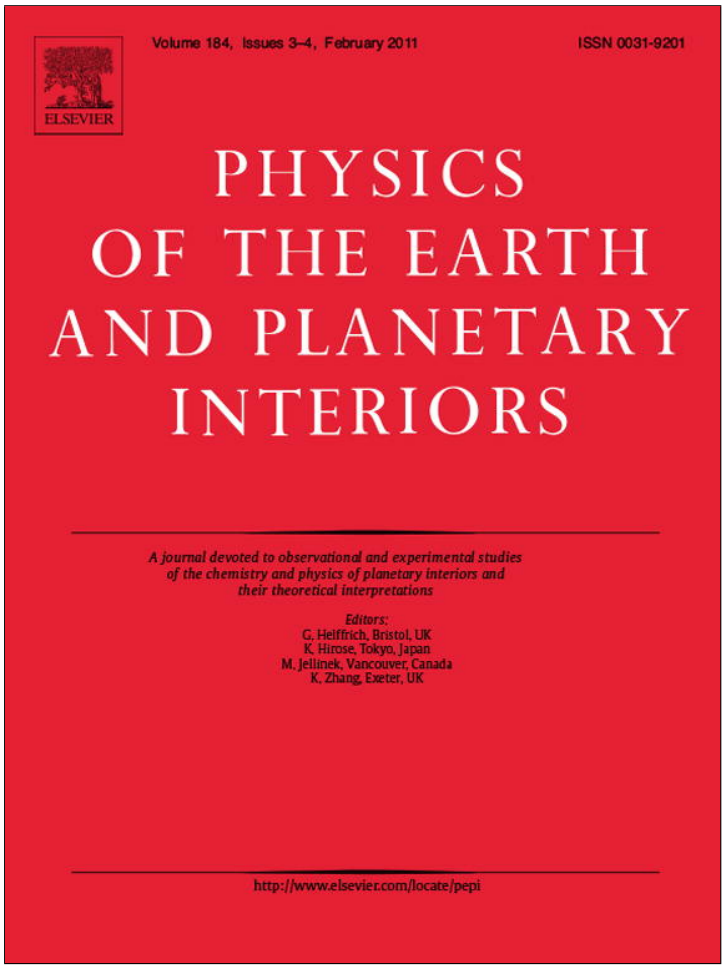

Physics of the Earth and Planetary Interiors 184 (2011) 143–153

Contents lists available at ScienceDirect

Physics of the Earth and Planetary Interiors

journal homepage: www.elsevier.com/locate/pepi

Asymmetric deformation across the San Francisco Bay Area faults from GPS observations in Northern California

N. Houlié [a,b,*], B. Romanowicz [b]

[a] School of Earth and Environment, Maths/Earth and Environment Building, The University of Leeds, Leeds LS2 9JT, United Kingdom
[b] Berkeley Seismological Laboratory, University of California at Berkeley, 215, McCone Hall, Berkeley, CA 94720-4760, USA

ARTICLE INFO

Article history:
Received 18 January 2010
Received in revised form 2 November 2010
Accepted 9 November 2010

Edited by: M. Jellinek

Keywords:
San Andreas fault
Crustal deformation
Geodesy
Seismology
Elasticity
Seismic cycle

ABSTRACT

We show that geodetic data from the Bay Area Regional Deformation (BARD) network indicate asymmetric motion across the San Andreas fault in the San Francisco Bay Area (SFBA), resulting from a strong contrast in rigidity across the fault, as determined previously from seismological data. Assuming asymmetric motion across the fault, we determine the location and size of the maximum strain rate in the region. We find that, compared to the determination using a symmetric model of deformation, it is shifted eastward and its value increases from ~0.4 μstrain/yr to ~0.65 μstrain/yr. Such strain rate amplitudes are consistent with previous geodetic slip rate estimates. We confirm that the geological units located east of SAF are entrained by the motion of the Pacific Plate and that the San Andreas fault (SAF) is the real rheological limit between the Pacific and North-American Plates. The asymmetry of rheology constrained in this study implies the strain rate maximum in SFBA is likely located between SAF and the Hayward fault system. This also has implications for hazards in the northern SFBA, in particular on the Rodgers creek fault.

1. Introduction

The San Francisco Bay Area (SFBA) is one of the tectonically most deformed areas in the world. This deformation is the result of relative motion of the Pacific (PAC) and North-America (NAM) plates. A large part of the strain (75%) is accommodated along structures lying in a 50 km wide land stripe delimited by seismically active faults. This stripe of continental crust is composed of domains captured by either Pacific or North America plate motions (Irwin, 1990). The last major earthquake in the area occurred in 1989 (Loma Prieta earthquake) (Segall and Lisowski, 1990; Dietz and Ellsworth, 1990; Ańadóttir and Segall, 1994). The deformation field after this large earthquake was perturbed (Argus and Lyzenga, 1994; Lienkaemper et al., 1997, 2001; Langenheim et al., 1997) and the microseismicity significantly increased since then in the southern portion of the SFBA. Today, in the SFBA, at least two major seismic events ($M_w \geq 6.5$) are expected along the San Andreas (SAF) and Hayward faults (HAY) within the next decades (Working Group on California Earthquake Probabilities, 2003). Interaction between earthquakes on Bay area faults is likely to be an important factor in the timing of Bay Area earthquakes (Pollitz and Nyst, 2005). As the prediction of the next large earthquake is based on the estimation of the stress accumulated across active faults (San Andreas, Hayward, Rodgers Creek, Calaveras (CAL), Green Valley fault, Greenville fault), it is important to quantify the strain rate amplitude and locate the strain rate peak across these faults. Several seismic studies have shown that a strong seismic velocity contrast exists in the crust across the San Andreas and Hayward faults (Uhrhammer, 1981; Thurber et al., 2007). This velocity contrast indicates a difference in elastic rheology between geological units located in the distributed deformation zone between the North America and Pacific plates. A greater inferred rigidity suggests that the PAC plate may be less deformed than blocks east of SAF.

The strain rate amplitude is logically the preferential parameter to measure with a GPS network as it can be inferred by measuring distances between two receivers at two epochs. In order to investigate the deformation over the BARD network, we have tied our network solution to the Pacific plate, which is mostly exempt from seismicity at the San Francisco latitude, rather than to a reference site. This allows us to tie the deformation profile to a site that is the closest to a stable reference tectonic object without impacting the inferred deformation distribution by any rotation or local effect at the reference site.

We consider asymmetric deformation across a fault. In this case, the maximum strain rate amplitude is not located above the fault trace as predicted in the standard symmetric case (Thatcher, 1986), and the distribution of strain rate is different. Larger deformation values are expected far from the fault trace. The change of the

* Corresponding author at: School of Earth and Environment, Maths/Earth and Environment Building, The University of Leeds, Leeds LS2 9JT, United Kingdom. Tel.: +44 1133436620.
E-mail addresses: houlie@seismo.berkeley.edu, n.houlie@leeds.ac.uk (N. Houlié).

0031-9201/$ – see front matter © 2010 Elsevier B.V. All rights reserved.
doi:10.1016/j.pepi.2010.11.003

location of the maximum strain rate impacts estimates of recurrence time for large earthquakes. In the SFBA tectonic setting, where large faults are producing overlapping deformation fields, motion on the SAF fault could accelerate or inhibit rupture on HAY or CAL faults. Such asymmetry of deformation could be generated by a combination of factors including dipping faults at depth (Jolivet et al., 2008) or geological discontinuities resulting from the long term displacement along the fault. Finally, testing the asymmetry of the motion is a unique opportunity to link the velocity models used in seismic tomography or moment tensor inversions with geodetic surface observations.

The asymmetry hypothesis was already considered by both geodesists (Lisowski et al., 1991) and seismologists (e.g. Uhrhammer, 1981; Le Pichon et al., 2005) and successfully applied to fault systems in southern California (Schmalzle et al., 2006). It has never been tested in the SFBA on a large geodetic dataset. We evaluate the velocity field in the light of this hypothesis. We also discuss the implications of the new location of the strain rate peak from the perspective of a future earthquake. Additionally we provide some elements on the geometry of tectonic features in the San Pablo Bay region.

We base our study on the GPS velocity field computed by using data from the Bay Area Regional Deformation (BARD) network (Table 1) (Romanowicz et al., 1994), including the recently installed "*mini-PBO*" sites (Fig. 1). Dedicated to monitoring deformation in Northern California, BARD provides data with which we can investigate the spatial distribution of the strain accumulation, the motion along faults and any unexpected transient deformation that would be related to seismic events (acceleration along the fault, landslides, hydrogeological features). Our study area will be limited in this work to the San Francisco Bay Area (SFBA).

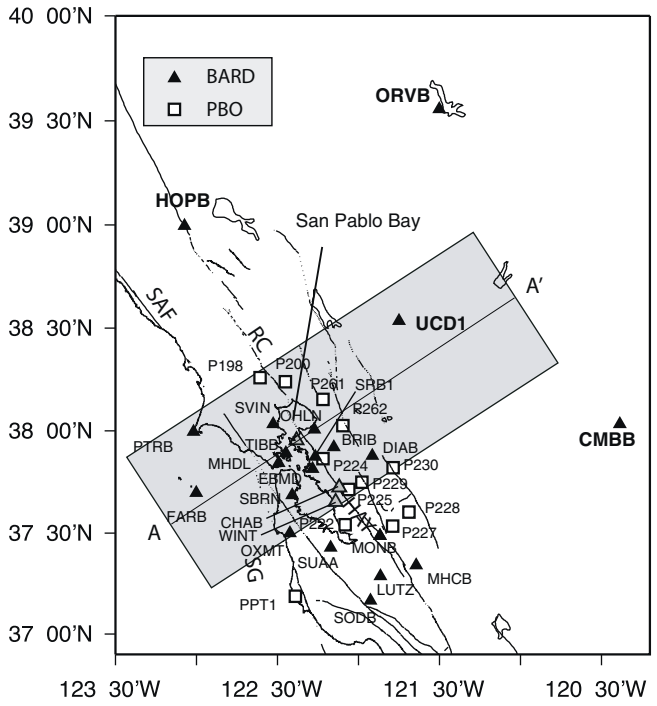

Fig. 1. Map of the permanent GPS benchmarks of the BARD (black triangles) and PBO (white squares) networks. The sites HCRO (Hat Creek Radio Observatory), PKDB (Parkfield, CA), SAOB (San Andreas Geophysical Observatory) and YBHB (Yreka Blue Horn Mine, CA) are located outside the map. SAF: San Andreas fault, RC: Rodgers Creek fault, HAY: Hayward fault, and SG: San Gregorio fault. The shaded area represents the width of the profile presented in Fig. 4.

2. Data

The BARD network is a permanent GPS network comprising 40 GPS sites, installed since 1992 in Northern California (King et al., 1994). The receivers installed are mainly Ashtech (Z-12 and μZ) and Trimble receivers (TR4000) with Choke Ring antennas. During the last two years, some of the receivers have been upgraded to Trimble NETRS with high-rate capabilities. Data are telemetered to the Berkeley Seismological Laboratory in real-time (sampling rates of 15 s or 1 s, depending on the station, and 3 s latency)

Table 1
List of the BARD stations maintained by the BSL. Five receiver models are operating now: Trimble 4000 SSE (T-SSE), Trimble 4000 SSI (T-SSI), Trimble NETRS, (T-NETRS), Ashtech Z12 and Ashtech Micro Z (A-UZ12). The telemetry types are listed in column 6. FR = Frame Relay, R = Radio, Mi = Microwave, WEB = DSL line, NSN = US National Seismic Network (VSAT: satellite telemetry). Some sites are transmitting data over several legs with different telemetry.

	Site	Lat.	Lon.	Receiver	Tele.	Rate	Co. Net.	Location
1	BRIB	37.91	237.84	NETRS	T1	1 Hz	BDSN	Orinda
2	CMBB	38.03	239.61	A-UZ12	FR	1 Hz	BDSN	Columbia
3	DIAB	37.87	238.08	A-Z12	FR	1 Hz		Mt. Diablo
4	FARB	37.69	236.99	A-Z12	R-FR/R	1 Hz	BDSN	Farallon Island
5	EBMD	37.81	237.71	T-5700	R	1 Hz		East Bay Mud
6	HOPB	38.99	236.92	TR 4000	FR	1 Hz	BDSN	Hopland
7	LUTZ	37.28	238.13	A-Z12	FR	30 s		Santa Clara
8	MHCB	37.34	238.35	A-Z12	FR	1 Hz	BDSN	Mt. Hamilton
9	MHDL	37.84	237.50	NETRS	FR	1 Hz	MiniPBO	Marin Headland
10	MODB	41.90	239.69	A-UZ12	NSN	1 Hz		Modoc Plateau
11	MONB	37.48	238.13	A-Z12	FR	1 Hz		Milpitas
12	MUSB	37.16	240.69	A-Z12	R-Mi-FR	30 s		Musick Mt.
13	OHLN	38.00	237.72	A-UZ12	FR	1 Hz	Mini-PBO	Ohlone Park, Hercules
14	ORVB	39.55	238.49	A-Z12	FR	1 Hz	BDSN	Oroville
15	OXMT	37.49	237.57	A-UZ12	FR	1 Hz	Mini-PBO	Ox Mountain
16	PKDB	35.94	239.45	A-Z12	FR	1 Hz	BDSN	Parkfield
17	PTRB	37.99	236.98	A-Z12	R-FR	1 Hz		Point Reyes Lighthouse
18	SAOB	36.76	238.55	A-Z12	FR	1 Hz	BDSN	Hollister
19	SBRN	37.68	237.58	A-Z12	FR	1 Hz	Mini-PBO	San Bruno
20	SODB	37.16	238.07	A-Z12	R-FR	15 s		Soda Springs, Los Gatos
21	SRB1	37.87	237.73	T-SSE	FR	1 Hz		Berkeley
22	SUTB	39.20	238.17	A-Z12	R-FR	1 Hz	BDSN	Sutter Buttes
23	SVIN	38.03	237.47	A-UZ12	FR	1 Hz	Mini-PBO	St Vincents
24	TIBB	37.89	237.55	A-UZ12	R	1 Hz		Tiburon
25	UCD1	38.53	238.24	NETRS	WEB	1 Hz		UC-Davis
26	YBHB	41.73	237.28	A-Z12	FR	1 Hz	BDSN	Yreka
27	UCSF	37.75	237.55	NETRS	FR	1 Hz		UC-San Francisco

Fig. 2. Permanent GPS sites included in the BARD processing since 1994. Velocities are presented in Table 3.

(Romanowicz et al., 1994). All the data are archived at the Northern California Earthquake Data Center (NCEDC, http://www.ncedc.org) (Neuhauser et al., 2001). The BARD network has operated long enough to provide velocities with millimeter accuracies in the San Francisco Bay Area (Blewitt and Lavallée, 2002).

All the data have been processed using the GAMIT/GLOBK tool suite (King and Bock, 2006; Herring, 2005). We have adjusted all the 4018 daily solutions using five reference sites (BAY1, GOLD, JPLM, PPT1, VNDP) that are present in our dataset and included in the International Terrestrial Reference Frame (ITRF 2000) release (Altamimi et al., 2002). The adjustment of the whole dataset of daily solutions was succesfully completed by minimizing the shift between the ITRF 2000 velocities and our solutions (Table 2). We present the set of sites included in this processing in Fig. 2. The computing strategy used in this study has been successfully applied in previous studies involving both short and long baselines (Houlié et al., 2006; Trota et al., 2006).

All the velocity residuals misadjustments with ITRF2000 are less than 1 mm/yr. Two sites (FARB and PTRB) are located west of SAF. The velocities computed are in good agreement with both local (Prescott et al., 2001; Savage et al., 1999), regional (d'Alessio et al., 2005) and global solutions (Sella et al., 2002) previously released. Our network scale solutions are thus robust. For the purpose of statistical estimation of robustness, we attribute to our velocity solutions an arbitrary error of 2 mm/yr. Formal errors are listed in Table 3.

3. Results

The low residuals at the PTRB and FARB with respect to the PAC (Fig. 3) indicate that there are no significantly active faults between these sites and the rest of the Pacific plate. This validates the choice of working in a PAC reference frame. We are thus able to tie the deformation profile to the geological units lying west of SAF.

We use the asymmetric dislocation model proposed by (Le Pichon et al., 2005) with a fault located at $x = 0$:

$$v(x) = s_1 + 2\frac{s_2}{\pi}\tan^{-1}\left(\frac{x}{D}\right); \quad x \geq 0 \tag{1}$$

$$v(x) = s_1 + 2\frac{s_1}{\pi}\tan^{-1}\left(\frac{x}{D}\right); \quad x < 0 \tag{2}$$

where s_1 and s_2 are the half velocities on the east and west sides of the fault, respectively, D is the locking depth of the fault, and x is the distance from the fault. In the symmetric case, $s_1 = s_2 = s/2$. Following this formalism, the velocity profile steepens eastward of the fault considered, as rigidity decreases. The velocity amplitudes expected are positive on both sides.

Since the SAF and HAY are close to each other (~30 km), it is impossible to model the effects of the two structures in the SFBA independently. We combine the deformation curves for SAF and HAY to obtain a velocity profile expected from the motion along the two faults. In particular, we were not able to test the asymmetry hypothesis along HAY alone because the monument quality of CHAB and WINT sites was poor (these sites are not located on bedrock) and the PBO network in the area is not mature enough to provide accurate long-term velocities (Blewitt et al., 2006).

Also, the amplitude of motion across a fault depends on the locking depth of the fault. Our velocity field is not sensitive enough to constrain the locking depths of SAF and HAY from our observations. In order to do this, more offshore GPS sites would be necessary. We therefore assume a locking depth of 10 km for both faults and later discuss the impact of this assumption on our results. We consider a section (Fig. 4) perpendicular (Azimuth N55) to the SAF and HAY and compute a set of expected velocity profiles (Fig. 4) using Eqs. (1) and (2), based on slip rate estimates (Lisowski et al., 1991; Chen and Freymueller, 2002; Prescott et al., 2001; d'Alessio et al., 2005). We confirm that the velocities are, respectively, 20 and 10 mm/yr across the SAF and HAY. The remaining 10 mm/yr of relative motion between PAC and Great Valley is attributed primarily to the Calaveras and Greenville faults (Prescott et al., 2001).

The slip rate along a fault inferred from the observation of deformation at the surface is tightly linked to the locking depth of the sliding fault. In order to assess the sensitivity of asymmetry to locking depths of SAF and HAY, independently of slip rates, we used a forward modelling approach that allows us to quantify the number of models that satisfy the observed velocity profile at the latitude of SF for each possible asymmetry parameter (from 0.3 to 1.5, where $s_1 = \alpha s_2$). According to the complexity of the fault system east of Hayward, since the GPS network may not be dense enough, the asymmetry across HAY has been fixed to 1.

Table 2
Discrepancies between previously published velocity values and recomputed values. The velocity adjustments dV_e and dV_n are computed with respect to ITRF2000. Most of these adjustments are smaller than a millimeter per year. Such error on sites, that demonstrate their stability over decades, shows the real accuracy of newer permanent sites is likely to be better than 1 mm/yr.

Sites	Lon. (deg.)	Lat. (deg.)	dV_e (mm/yr)	dV_n (mm/yr)	Reference frame
BAY1	197.293	55.19	−0.03	0.01	ITRF2000
GOLD	243.111	35.425	1.20	−0.11	ITRF2000
JPLM	241.827	34.205	0.50	0.59	ITRF2000
PPT1	237.61	37.187	0.82	0.27	ITRF200
VNDP	239.384	34.556	−0.05	−0.81	ITRF2000

Table 3
GPS velocities for permanent sites used in this study. We indicated BARD and cooperative BARD site (such as EBMD with East Bay Mud District Utility in Oakland) with a star. Other sites are used in order to stabilize the adjustment of the velocity on the long-term.

Lon. (deg.)	Lat. (deg.)	V_e (m/yr)	V_n (m/yr)	S_e (mm/yr)	S_n (mm/yr)	Site
297.660	82.494	−0.0191	−0.00266	0.3	0.3	ALRT
291.737	49.187	−0.01335	−0.00129	0.29	0.28	BAIE
263.998	64.318	−0.01283	−0.00971	0.29	0.28	BAKE
237.847	37.919	−0.01947	−0.00018	0.27	0.28	BRIB
295.304	32.370	−0.00855	−0.00034	0.28	0.28	BRMU
4.359	50.798	0.01422	0.0098	0.27	0.27	BRUS
26.126	44.464	0.01909	0.00945	0.25	0.28	BUCU
237.881	37.724	−0.02012	0.0023	0.27	0.28	CHAB
238.335	39.433	−0.01558	−0.00913	0.27	0.28	CHO1
265.911	58.759	−0.0121	−0.00972	0.28	0.28	CHUR
239.614	38.034	−0.01562	−0.00599	0.27	0.28	CMBB*
235.604	40.442	−0.03355	0.01144	1.75	1.08	CME1
239.000	37.641	−0.01377	−0.00514	0.39	0.38	CMOD
238.722	37.896	−0.01767	−0.00848	0.27	0.28	CNDR
238.084	37.879	−0.01653	−0.00517	0.27	0.28	DIAB*
265.71	34.111	−0.00709	−0.00869	0.42	0.31	DQUA
237.716	37.815	−0.02346	0.007	0.27	0.28	EBMD*
293.008	44.909	−0.01128	−0.00122	0.28	0.28	EPRT
295.201	47.073	−0.0125	0.00099	0.47	0.4	ESCU
236.999	37.697	−0.03269	0.0207	0.27	0.28	FARB*
258.022	54.726	−0.01117	−0.01313	0.28	0.28	FLIN
243.111	35.425	−0.01215	−0.00949	0.27	0.28	GOLD
6.921	43.755	0.01985	0.01421	0.53	0.44	GRAS
15.493	47.067	0.01815	0.01436	0.52	0.44	GRAZ
238.53	40.816	−0.01083	−0.01143	0.28	0.28	HCRO
296.389	44.684	−0.01225	−0.00053	0.29	0.28	HLFX
242.239	70.736	−0.0102	−0.01594	0.28	0.28	HOLM
236.925	38.995	−0.02365	0.00447	0.27	0.28	HOPB*
276.489	49.667	−0.0128	−0.00743	0.3	0.28	HRST
226.473	68.306	−0.00394	−0.01801	0.28	0.27	INVK
30.096	62.391	0.01487	0.00858	0.26	0.28	JOEN
241.827	34.205	−0.03079	0.00842	0.27	0.28	JPLM
8.411	49.011	0.01627	0.01126	0.27	0.27	KARL
309.055	66.987	−0.01653	0.00396	0.28	0.27	KELY
135.046	48.521	0.02202	−0.0104	0.34	0.31	KHAJ
21.06	67.878	0.01048	0.00995	0.27	0.27	KIR0
282.255	55.278	−0.01343	−0.00696	0.3	0.28	KUUJ
238.135	37.287	−0.02477	0.00684	0.27	0.28	LUTZ*
17.259	60.595	0.01295	0.00937	0.27	0.27	MAR6
24.395	60.217	0.01509	0.00908	0.26	0.27	METS
238.357	37.342	−0.01726	−0.00516	0.27	0.28	MHCB*
239.697	41.902	−0.00949	−0.01208	0.28	0.28	MODB*
237.58	37.947	−0.02329	0.00708	0.27	0.28	MOLA*
238.133	37.485	−0.02046	−7e−05	0.27	0.28	MONB*
358.315	55.213	0.0122	0.01047	0.27	0.27	MORP
240.691	37.170	−0.01545	−0.00734	0.27	0.28	MUSB*
298.311	56.537	−0.01386	0.00221	0.29	0.28	NAIN
284.376	45.454	−0.01193	−0.00419	0.28	0.28	NRC1
88.360	69.362	0.01721	0.00272	0.29	0.32	NRIL
237.727	38.006	−0.0196	0.00123	0.27	0.28	OHLN*
238.500	39.555	−0.01533	−0.00951	0.27	0.28	ORVB*
237.576	37.499	−0.03002	0.01487	0.27	0.28	OXMT*
237.623	37.915	−0.02323	0.00689	0.31	0.31	P181
237.393	38.26	−0.02186	0.0071	0.29	0.29	P198
237.497	38.264	−0.01765	0.00342	0.29	0.29	P199
237.548	38.240	−0.02017	0.00239	0.29	0.29	P200
237.917	37.539	−0.02484	0.00821	0.29	0.29	P222
237.942	37.714	−0.02149	0.00086	0.29	0.29	P225
238.210	37.533	−0.01862	−0.00407	0.29	0.3	P227
238.313	37.602	−0.01679	−0.00429	0.29	0.29	P228
238.022	37.749	−0.02007	−0.00136	0.29	0.29	P229
238.214	37.819	−0.01742	−0.00737	0.29	0.29	P230
237.782	38.153	−0.01759	0.00016	0.29	0.29	P261
239.458	35.945	−0.03908	0.0164	0.27	0.28	PKDB*
237.610	37.187	−0.03295	0.01919	0.27	0.28	PPT1
245.707	50.871	−0.00787	−0.01685	0.28	0.28	PRDS
236.981	37.996	−0.03065	0.01955	0.27	0.28	PTRB*
255.654	38.287	−0.00653	−0.01228	0.36	0.3	PUB1
313.952	60.715	−0.0153	0.00673	0.29	0.27	QAQ1
295.966	67.559	−0.01706	0.0008	0.35	0.31	QIKI
265.106	74.691	−0.01167	−0.01028	0.31	0.31	RESO
338.045	64.139	−0.01277	0.01333	0.28	0.26	REYK
24.059	56.949	0.01546	0.00957	0.26	0.27	RIGA
238.442	37.667	−0.01576	−0.00698	0.28	0.28	S300*
238.553	36.765	−0.03416	0.01882	0.27	0.28	SAOB*

Table 3 (*Continued*)

Lon. (deg.)	Lat. (deg.)	V_e (m/yr)	V_n (m/yr)	S_e (mm/yr)	S_n (mm/yr)	Site
13.643	54.514	0.01453	0.0117	0.35	0.3	SASS
237.59	37.686	−0.02501	0.01099	0.27	0.28	SBRN*
293.167	54.832	−0.01498	−0.00088	0.28	0.28	SCH2
203.39	71.323	0.0047	−0.02034	0.32	0.29	SG27
26.389	67.421	0.01203	0.00865	0.27	0.27	SODA
238.074	37.166	−0.02643	0.00925	0.27	0.28	SODB*
307.322	47.595	−0.01308	0.00453	0.28	0.27	STJO
237.827	37.427	−0.02677	0.00978	0.27	0.28	SUAA*
238.179	39.206	−0.01574	−0.00956	0.27	0.28	SUTB*
237.474	38.033	−0.02394	0.00754	0.27	0.28	SVIN*
238.065	37.351	−0.02357	0.00723	0.27	0.28	THAL*
237.552	37.891	−0.02383	0.00856	0.27	0.28	TIBB*
254.767	40.131	−0.00817	−0.01291	0.28	0.28	TMGO
18.940	69.663	0.00925	0.01114	0.27	0.27	TRO1
238.249	38.536	−0.0159	−0.00872	0.27	0.28	UCD1*
293.358	45.950	−0.01244	−0.00104	0.28	0.28	UNB1
18.367	57.654	0.01466	0.00949	0.27	0.27	VIS0
239.384	34.556	−0.03574	0.01884	0.28	0.28	VNDP
237.859	37.653	−0.02389	0.00679	0.27	0.28	WINT
267.985	46.705	−0.01101	−0.00983	0.28	0.28	WIS1
237.289	41.732	−0.00809	−0.00957	0.28	0.27	YBHB*

The number of parameters is equal to 5: two locking depths, two slip rates and one asymmetry parameter. Besides, as the two faults are modelled together, some values are strongly unlikely (i.e. the sum of slip rate must be close to 40 mm/yr, Freymueller et al., 1999). We compute a velocity profile for each value of the 5 parameters within the ranges (Table 4) proposed by Working Group on California Earthquake Probabilities (2003) to estimate the agreement with observations for various values of asymmetry α (from 0.3 to 1.5).

For each of the 8190 models, we compute the *RMS* value of modelled velocity profiles for both SAF and HAY. The values explored in this study are listed in Table 4.

Table 4
Parameters of SAF and HAY faults explored during the statistical analysis of the results. These parameters have been published by Working Group on California Earthquake Probabilities (2003). We computed models for every value of *alpha* from 0.3 to 1.5.

Fault locking depths (km)	Slip rate (mm/yr)	
	90% bounds	95% bounds
North San Andreas	9–13	21–27
North Hayward	10–14	7–11

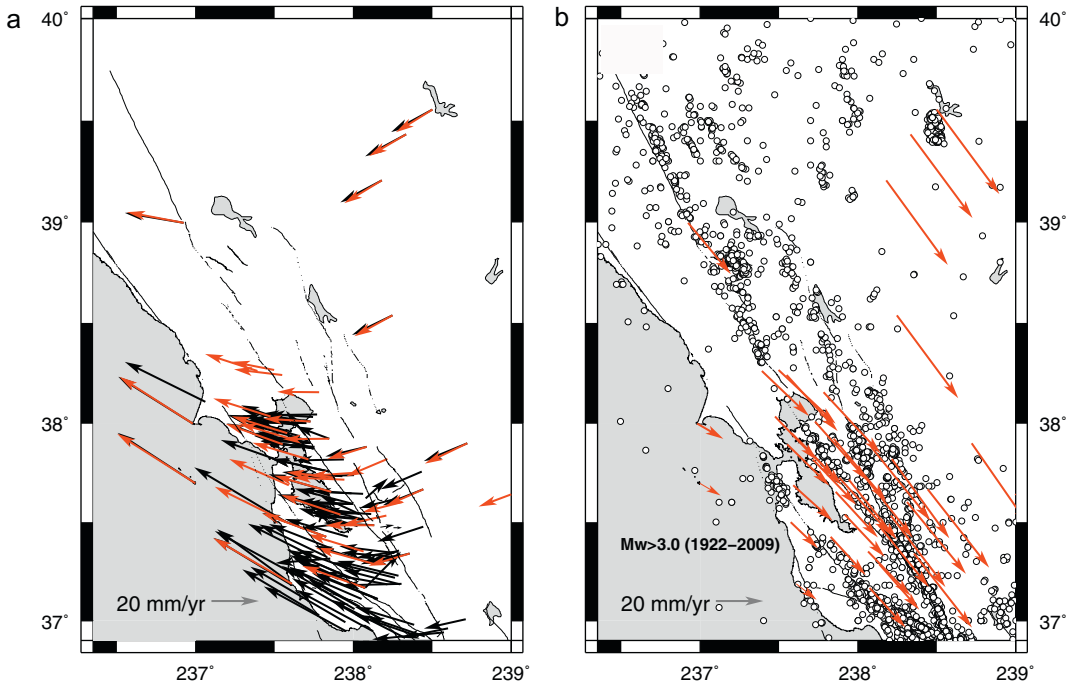

Fig. 3. (a) Comparison of the absolute velocity field solutions for two different studies. The agreement of BAVU solutions (black arrows) with BARD permanent solutions is good. This reflects the good adjustment of campaign solutions with those based on permanent sites. We did not use the BAVU dataset as these datasets are too heterogeneous (i.e. troposphere sampling, duration of sessions, number of sites, number of permanent sites used). (b) BARD velocity field (1994–2007) in the SFBA with respect to the motion of the Pacific plate (Sella et al., 2002). All velocity formal errors are less than 1 mm/yr. The small motion of the sites FARB and PTRB suggests that the western side of the San Andreas fault is not deformed by the motion along the SAF and SG faults. The seismicity (1988–2006 from Advanced National Seismic System (ANSS) catalog http://www.ncedc.org/anss/) supports the inference that blocks west of SAF are less deformed than the SFBA and the continental domains. The low seismicity also supports a stronger rheology west of the San Andreas fault.

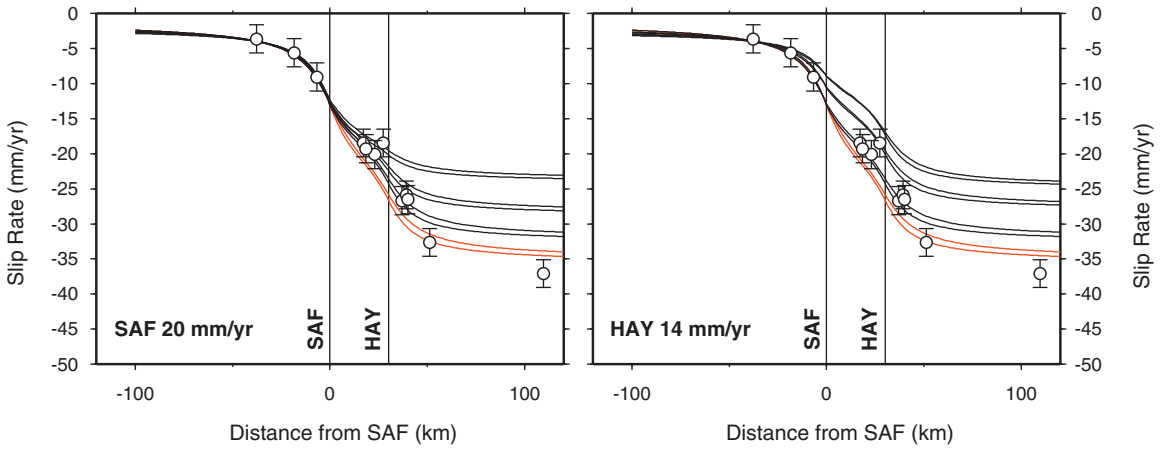

(a) Creep along HAY is neglected

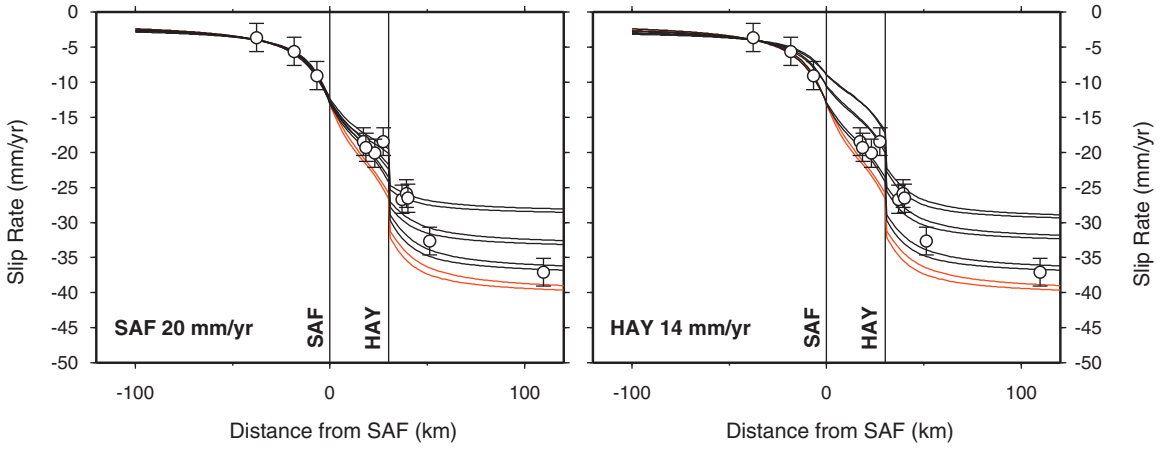

(b) Creep along HAY = 5 mm/yr

Fig. 4. Comparison between contributions of the SAF and HAY motions in the Bay Area with respect to PAC. (a) Velocity profiles including 30% asymmetry (in black) and without asymmetry (in red) have been computed for locking depths equal to 10 and 12 km. On each panel, we fix the velocity across one of the faults and vary the contribution of motion across the other fault. We first computed the velocities profiles (top plots) for SAF 20 mm/yr with HAY equal to 5, 8 and 14 mm/yr. We then adjusted the slip rate of SAF (5, 10 and 20 mm/yr) assuming HAY slip rate was equal to 14 mm/yr. For this first set of models, the creep contribution is not considered. (b) Same as (a) except we added 5 mm/yr of creep along HAY. We note that a large range of models fits the velocity data at the latitude of SF. These plots suggest the sip rate along SAF is close to 20 mm/yr while the slip rate of HAY remains unknown because the creep component is masking the elastic deformation close to HAY. However, it seems the creep component favors low slip rates for HAY and a large asymmetry across SAF. (For interpretation of the references to color in this figure legend, the reader is referred to the web version of the article.)

We quantify the quality of each model by computing an *RMS* value of the misfit as follows:

$$RMS = \sqrt{\frac{1}{N}\sum \frac{(V_{obs} - V_{model})^2}{\sigma^2_{V_{obs}}}} \quad (3)$$

where $\sigma_{V_{obs}}$ is the error on the observations (fixed to 2 mm/yr), V_{obs} is the longitudinal velocity and V_{model} the value predicted by the model. N is the number of sites modelled along the considered profile (Fig. 1). In this study, $N = 11$.

To avoid to favor a non-unique model, we work with the best 200 models with lowest RMS ($1.26 < RMS < 1.76$). The distribution of good models versus the parameter α is unimodal (Fig. 5). We see the distribution of the RMS versus α is not centered at $\alpha = 1$ and that there are more models with higher rather than smaller values of α. According to this observation, we can distinguish a group of models with $0.6 < \alpha < 1.2$. This group of models have a frequency of occurrence close to 50% (1 model out of 2 in total) for each value of α tested.

To check the stability of the distribution, we also plot the same figure for the best 50 and 100 models (Fig. 5a and b). As the number of models could be too small to establish reliable statistics of the parameter α with 50 or 100 models, we continue to work with the best 200 models.

In order to discriminate between the models, we considered their consistency with previous work. For this, we tested the values of locking depths and slip rates along the HAY and SAF fault versus α for these 200 models. We plot this relationship in Fig. 6. We note there is no relationship between the locking depth of both HAY and SAF or slip rate of HAY with the parameter α. However, there is a clear linear relationship between the SAF slip rate and the parameter α. This is true for both the 200 best models or the selection of models with ($0.6 < \alpha < 1.2$, indicated by darker symbols in Fig. 6).

Additionally, our results indicate the constraint on the SAF locking depth at the latitude of San Francisco for the best 200 models is quite strong. Indeed, none of the selected models were able to reproduce the observed distributed motion with a different locking depth. This indicates that while the values of α can be diverse, the locking depth has to be close to 10 km. In this case, we can-

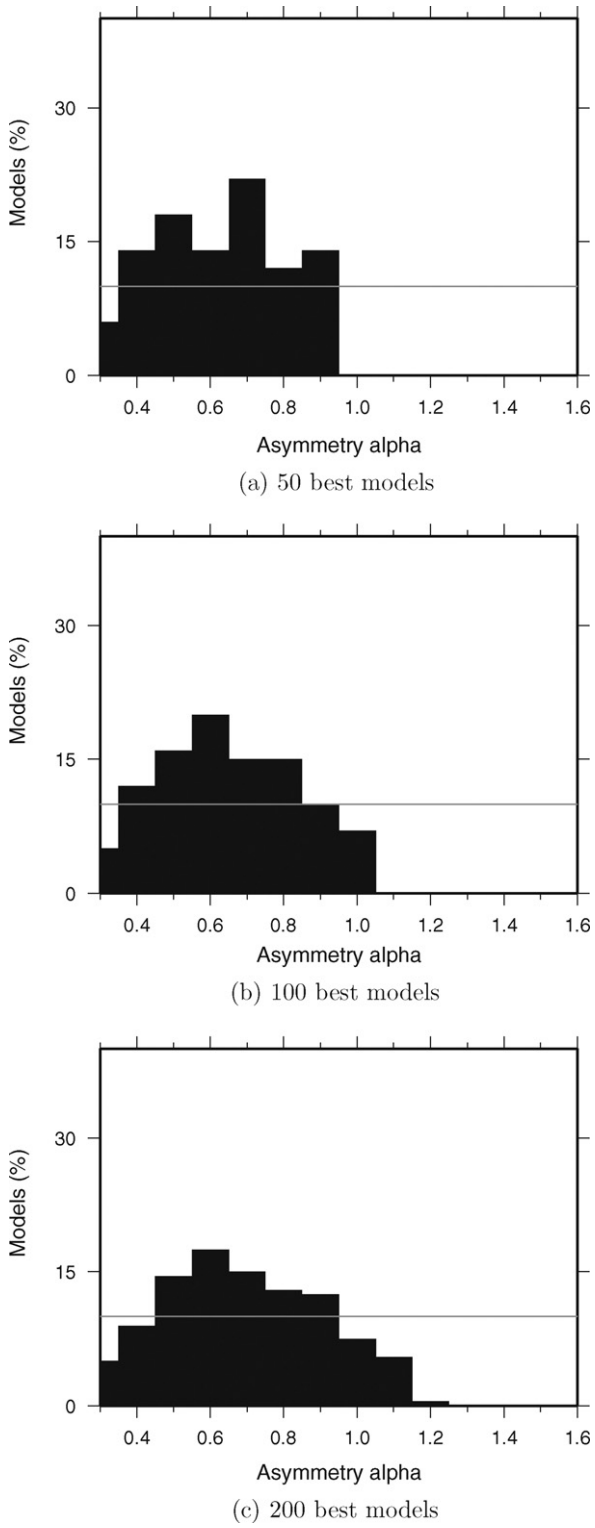

Fig. 5. Distribution of alpha for the best 50, 100 and 200 models. The distribution is slighty asymmetric with more models for large values of α. We indicated the level of 10% occurrence with a grey line. More than >60% of the models have a alpha value between 0.6 and 0.9.

not describe a error for this parameter, but we assume it should be smaller than 1 km. This value of 10 km for the locking depth is consistent with the values provided by by (Working Group on California Earthquake Probabilities, 2003).

We then plot the half slip rate for SAF versus α in Fig. 6 (top right). We note that for the last two parameters (the locking depth and the slip rate of HAY), the resolution is very poor. This is largely due to the poor availability of data west of HAY at the time of the processing. When the PBO network becomes mature, we will be able to better resolve these parameters.

Finally, we plot the number of good models in the space of parameters explored (Fig. 7). This gives us the opportunity to show that the distribution of the models is quite different and the locking depth of HAY is the least constrained parameter of this study.

In the rest of the study we fix the SAF and HAY slip rate to 20 mm/yr and 10 mm/yr according to previous studies and our forward modelling analysis. Such a slip rate is reasonable and close to values provided in a large collection of studies (Working Group on California Earthquake Probabilities, 2003).

By adjusting the HAY and SAF theoretical velocity profiles (Fig. 4) to the observed velocity profile, we infer that s_1 and s_2 are, respectively, equal to 7 and 14 mm/yr for SAF (or 20 mm/yr of motion along the fault with 10 km locking depth). As the total strain energy stored along SAF has to be constant to fit the velocity observations, the deformation deficit on the western side is balanced by a deformation increase in the SFBA. This adjustment implies a rigidity contrast of ~30% across the SAF. This rigidity constrast is higher than the value proposed by Le Pichon et al. (2005) at Point Reyes (10%) but smaller than the rigidity constrast proposed by the same author at Point Arena (60%). Note that the obtained rigidity contrast is in agreement with seismological studies (Thurber et al., 2007).

We infer that the rheology of the PAC Plate is different from that of the continental area east of SAF and that both sides are differently deformed. In other words, the velocity field with respect to PAC thus supports the view that the rheology contrast (and its associated rigidity contrast) observed by structural geologists (Irwin, 1990) can be detected across the BARD network from West to East.

While the strain rate across the Hayward fault can be assumed symmetric above the fault trace because both sides of the fault are located within the continental tectonic unit, the strain rate profile across the San Andreas fault is thus pushed eastward, sharpening the profile of the total strain rate (contribution of both SAF and HAY) observed in the East Bay (Fig. 8). Both asymmetric and symmetric deformation related values are in agreement with the strain rates previously proposed (Thatcher, 1990; Kreemer et al., 2003). Thus asymmetric deformation along the SAF can explain the observed velocity profile across the SFBA at least as well as models assuming symmetric deformation across SAF and is consistent with seismological and geological observations of structural contrasts across the fault.

We can now include this asymmetry of deformation in order to quantify and relocate the maximum shear strain rate values in the Bay Area. The maximum change of velocity along the profile indicates its location. As the strain rate observed here is an indication of the preparation of seismic event(s) along one (or several) fault(s) (identified or not) in the SFBA during the seismic cycle, the location of the maximum amplitude of strain has an impact on the recurrence time between two large earthquakes.

By testing the rigidity μ (also estimated from seismic observations of P and S wave velocities across the deformed domain), we quantify the shear stress rate $\dot{\sigma}_s$ across the fault using the following relationship:

$$\dot{\sigma}_s = \mu \dot{\varepsilon}_s \tag{4}$$

A large earthquake occurs when the shear stress σ_s reaches a critical value $\sigma_s^{\max}$, where:

$$\sigma_s^{\max} = \int \dot{\sigma}_s \, dt \tag{5}$$

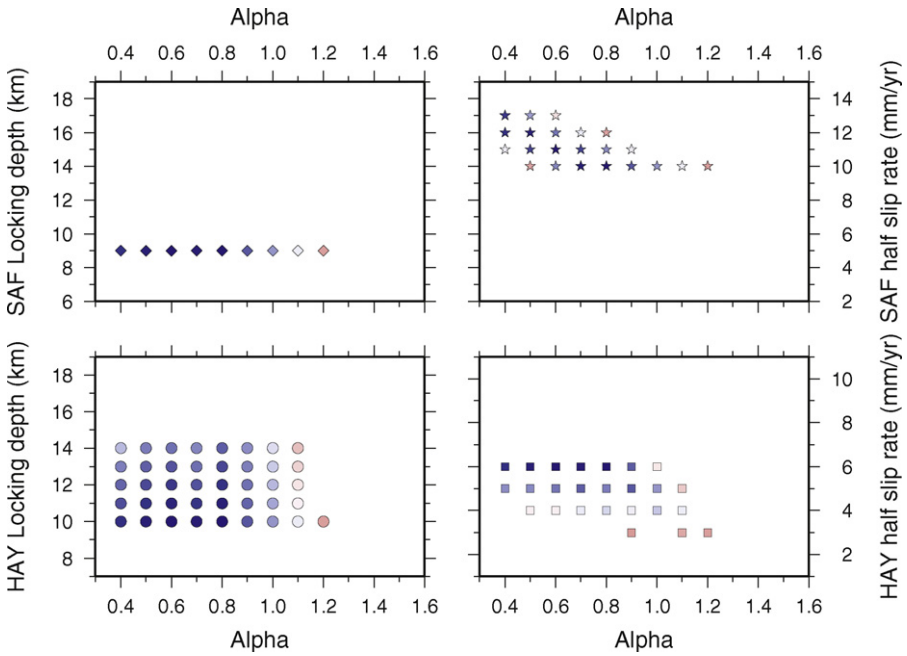

Fig. 6. Relationship between asymmetry parameter α, slip rates (right plots) and locking depths (left plots) for HAY and SAF for the best 200 models. We qualitatively indicate the lowest values of RMS color and the highest in red color. For this selection of models, the locking depth for SAF seems well constrained and does not depend on α but on the slip rate of the fault. The locking depth of HAY does not seem sensitive to α while low values of locking depths are favored by low values of α. However, a linear relationship between the parameter α and the SAF slip rate can be established. Smallest values of α favor models with large values of SAF slip rate. Largest values of HAY locking depths are preferably associated with the lowest values of α. This relationship will have to be revisited after the PBO sites velocities become statiscally robust. (For interpretation of the references to color in this figure legend, the reader is referred to the web version of the article.)

Hence

$$\sigma_s^{\max} = \int \mu \dot{\varepsilon}_s \, dt \tag{6}$$

Assuming all the energy accumulated during the seismic cycle is not released in any other manner than elastically, the cumulative shear stress over time is the value of the shear stress drop during the coseismic part of the seismic rupture. The maximum strain accumulated across a fault is directly linked to the recurrence time of large earthquakes on this fault (Fig. 8). The maximum stress slowly builds up from relative plate motion which we can measure using GPS. Since we know that the next earthquake will occur along the active faults, we can equal the maximum strain rate value to the shear angle rate. Constraining the strain rate value in the SFBA is thus a key element in order to estimate the time of the next large earthquake. Indeed, the uncertainty on the strain rate is linearly related to the recurrence time of the large earthquakes (Eqs. (5) and (6)). Assuming the recurrence time is 150 yrs (with $\mu = 3010^9$ Pa, Schön, 1996, and a strain rate value of 0.6 μstrain/yr), it is likely the shear stress accumulation in this area cannot be larger than 2.710^6 Pa over a full seismic cycle. Any error on the amplitude of the maximum shear strain will also impact the predicted time of the next large SAF earthquake. Assuming the maximum shear stress is known, an error of 0.2 μstrain/yr on $\dot{\varepsilon}$ will lead to an error on the recurrence time (Fig. 8) between large earthquakes from 10 to up to ∼30% (with 180 yrs seismic cycle duration, Goldfinger et al., 2008, years of seismic cycle duration change and assuming $\mu = 3010^9$ Pa) following strain observations made after large earthquakes (Thatcher, 1986).

After removing the contribution of the two faults to the original velocity field, we plot the residual velocities that may be due to a combination of other elastic inter-seismic motion along faults, creep and instabilities of sites (Fig. 9).

Three main features appear on the map of velocity residuals:

1. A motion across the San Gregorio fault: we cannot distinguish between an effect of creep (3 mm/yr) or that of elastic load (5 mm/yr). In any case, this confirms that the San Gregorio fault, known as the structure that participated in the 1906 earthquake nucleation (Geist and Zoback, 1999), is currently active (d'Alessio et al., 2005).
2. The contribution of creep across the Hayward fault (Fig. 10): we have plotted the creep estimates and compared them with seismic measurements (Bürgmann et al., 2000) and creepmeter measurements (Lienkaemper et al., 1997, 2001). We observe that the GPS estimates fit the seismic estimates better than the creepmeter measurements, in particular to the south where there is a discrepancy between the two datasets. This indicates that the GPS observations measure the interseismic deformation rather than near-surface damage. After plotting the residual displacements in the direction parallel to the fault (Fig. 9), we suggest that San Pablo Bay could be the place of future slip along HAY and a potential connection between HAY and Rodgers Creek fault could exist. The possibility that the next Hayward large earthquake will reach the northern shore of San Pablo Bay will increase the magnitude of the next large Hayward fault earthquake by 0.1 ($M_w = 7.1$) to 0.2 ($M_w = 7.2$) (light and dark grey in Fig. 10).
3. A motion across the Rodgers Creek fault: the relative motion between the PBO sites P198 and P200 is large enough to be attributed to either creep or interseismic deformation of similar amplitude to that observed across HAY (10 mm/yr slip). As in the San Gregorio case, the vector is so small, and the instrument coverage so poor that it is difficult to distinguish between creep and elastic load contributions.

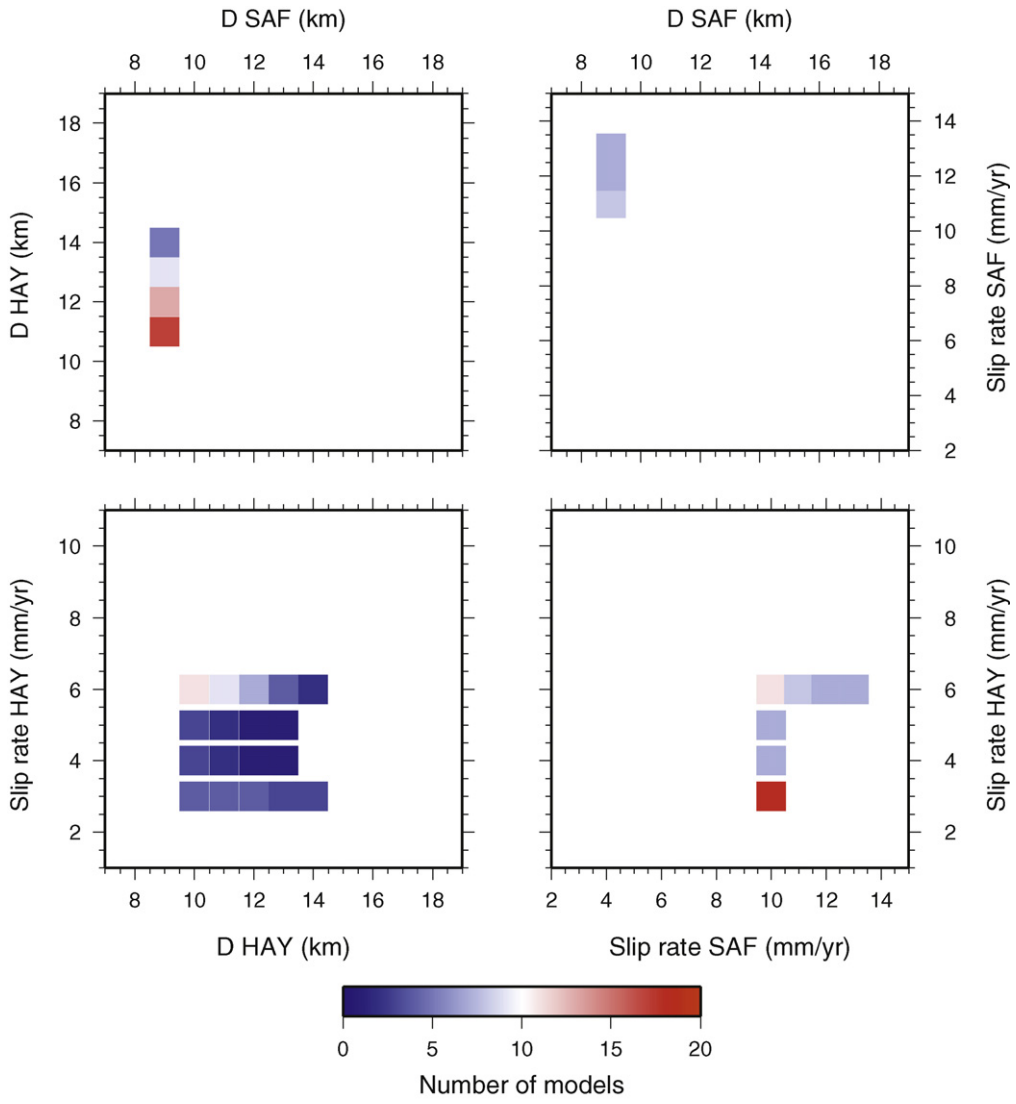

Fig. 7. Dependence of locking depth and slip rates of SAF and HAY on the number of good models (see text). We computed *RMS* value for every possible model. Velocities V_{SAF} and V_{HAY} are the less dispersed parameters. There is also a dependence of the locking depth of faults on asymmetry parameter α (top left panel). Small values of α are associated with small values of HAY locking depth D_{HAY} and smaller values of SAF slip rate V_{SAF}. We then used the best 15 models in order to compute errors on the parameters. Best values for D_{SAF}, D_{HAY}, V_{SAF} and V_{HAY} are, respectively, 9.00 ± 0.00 km, 11.73 ± 1.37 km, 11.41 ± 1.02 mm/yr and 5.22 ± 0.77 mm/yr. Half slip rate V_{SAF} is in good agreement with old and recent publications for northern segment of SAF. However, our model predicts a high value of slip rate for Hayward fault. We interpret this high value as an indication the creep component affects the fault in its entire thickness.

Our model is validated by the fact that our creep estimate (Fig. 10) on HAY is in good agreement with previous solutions (Bürgmann et al., 2000).

4. Discussion and conclusions

We have shown that the strain rate distribution in the SFBA is affected by the strong contrast between continental and oceanic domains. Small distances between a continental domain and an oceanic plate can be found in several places around the world (e.g. West coast of Canada, Southern America, and Japanese subduction) where asymmetric deformation profiles could be validated. However, with very rare exceptions, there is no example of permanent GPS instrumentation in areas where the contact between a continental and an oceanic plate is visible inland.

The asymmetry of the motion across the two active faults in the SFBA allows us to establish a connection between geodetic and seismic observations in the long term (>5 yrs). Good agreement between the static and dynamic elastic parameters is not usually observed on tectonically active volcanoes (Cayol and Cornet, 1998; Houlié, 2005). The maximum shear stress amplitude expected along the SAF (from 10 to 30 bars) is close to the values published for the 1906 earthquake (10–100 bars). Also, the peak location of strain rate is crucial to determine the gradient of deformation. Indeed, as SFBA faults are close to the time of rupture (we are at least in the middle of the seismic cycle for SAF and HAY), quantifying the gradient of deformation will help to constrain the characteristics of strain potentially able to trigger the next large earthquake in the area.

However, our assumption of isolated faults (SAF and HAY only) in the SFBA can be debated. The strain rate might need to be modelled at a finer scale (500 m or less) where geological evidence shows some of the strain can be partitioned across parallel faults. Such accuracy cannot be reached with the present density of the GPS network, which is not likely to be sensitive to structures at the 100 m scale.

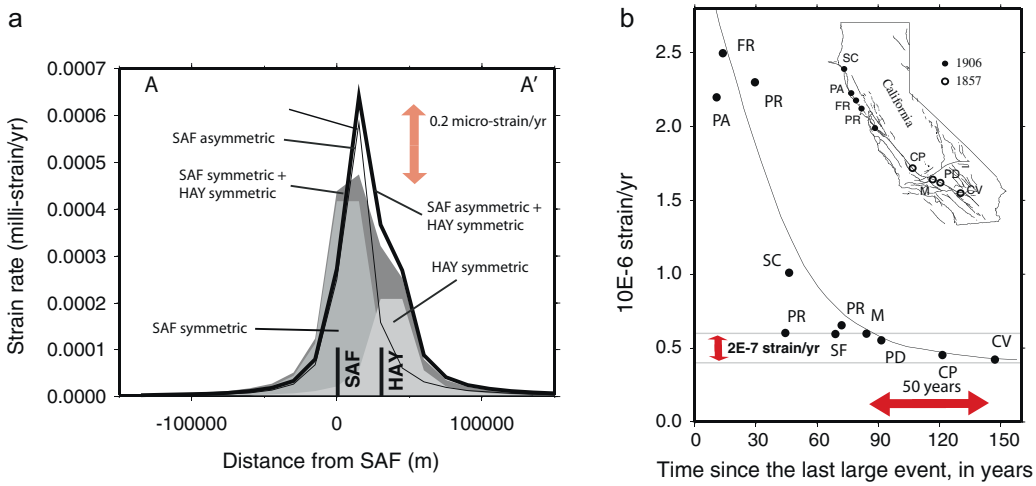

Fig. 8. Strain rate estimates along the profiles related to SAF and HAY faults only. (a) Strain rate across the San Francisco Bay Area. We have modelled the two strain rates regimes associated with the motions along a profile perpendicular to the San Andreas and Hayward faults. The regimes assuming symmetry across the San Andreas fault are indicated by grey areas while the new profiles are indicated with black lines. The asymmetry across the San Andreas fault pushes the strain rate eastward while its profile sharpens and increases from ~0.5 to ~0.65 μstrains/yr. The value of the SAF-parallel shear strain rate along the profile is linked to the shear stress building rate σ_s. (b) The strain rate $\dot{\varepsilon}$, as a function of the time since the last occurrence of a large earthquake along the SAF, indicates the load of the fault during the interseismic period. The accumulation of strain during the interseismic cycle prepares for the next mainshock. Thus, measuring it can help constrain the shear stress released during the mainshock, assuming the duration of the seismic cycle can be constrained. Also, if the strain rate is measured, its amplitude can help to infer what is the state of the fault today. This plot shows there is a link between the strain rate and the time recurrence of the large seismic events (Thatcher, 1990). However, as the maximum shear stress value leading to rupture on the fault is not known, the recurrence time between large earthquakes cannot be determined. We show here that an uncertainty of 0.2 μstrain/yr in the estimation of $\dot{\varepsilon}$ leads to an uncertainty of up to ~50 yrs in the recurrence time between two large earthquakes.
Figure modified from Thatcher (1990).

The description of the fault motion in the PAC reference frame opens the possibility of quantifying the asymmetry with other techniques such as InSAR, if defined in the new reference frame.

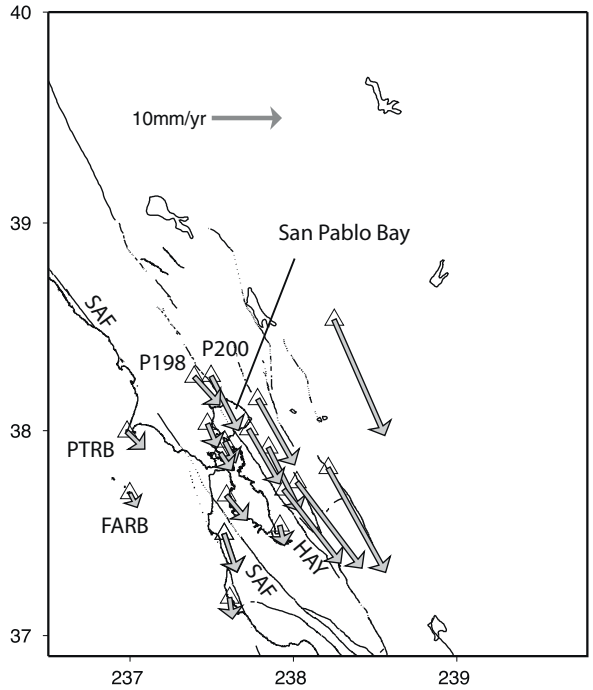

Fig. 9. Residual velocity field after removing the asymmetric contribution of the San Andreas fault. The slowdown of the motion from the south to the north is clearly visible. This confirms that the creep component along the Hayward-Rodgers Creek fault decreases toward the north.

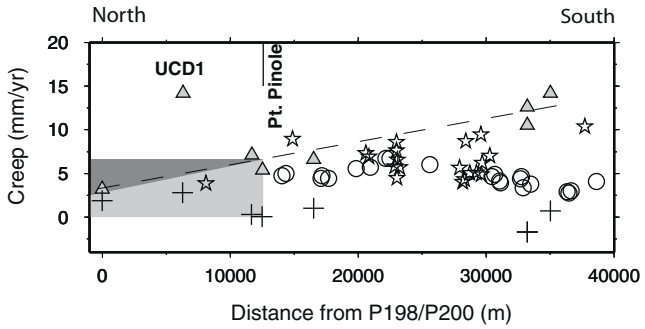

Fig. 10. Estimation of creep along Hayward fault. Creep estimates from different techniques along Hayward fault (stars: seismicity, Bürgmann et al., 2000; circles: creepmeters, Lienkaemper et al., 1997, 2001; triangles: our solution). As suggested by Bürgmann et al. (2000) our estimate (grey triangles) of the creep component is larger to the south but we note that this component is not expected to be equal to zero near Point Pinole of San Pablo with a value close to 5 mm/yr. Assuming the motion of the fault is unchanged across the San Pablo Bay to the north sites P198/P200, the energy accumulated along $12.5 \times 10.0\,km^2$ is missing from the seismic estimation based on the assumption the motion north of Point Pinole is close to zero. This underestimation of the fault motion leads to an error in the estimate of the energy released of about 30% (and 0.1 on the Magnitude M_w scale). Crosses indicate the residual velocities for sites located east of HAY after removing the effect of elastic load from both SAF and HAY.

Acknowledgements

The BARD network is partially supported by USGS through cooperative agreement 07HQAG0031 and by the University of California at Berkeley. The BSL contribution number of this study is 10-13.

References

Altamimi, Z., Sillard, P., Boucher, C., 2002. ITRF2000: terrestrial reference frame for earth science applications. J. Geophys. Res. 107 (B10), 2114, doi:10.1029/2001JB000561.
An′adóttir, T., Segall, P., 1994. The 1989 Loma Prieta earthquake imaged from inversion of geodetic data. J. Geophys. Res. 99 (B11), 21835–21856.

Argus, D., Lyzenga, G., 1994. Site velocities before and after the Loma Prieta and Gulf of Alaska earthquakes determined from VLBI. Geophys. Res. Lett. 21 (5), 333–336.
Blewitt, G., Kreemer, C., Hammond, W., Plag, H.-P., Stein, S., Okal, E., 2006. Rapid determination of earthquake magnitude using GPS for Tsunami Warning Systems. Geophys. Res. Lett. 33 (L11309), doi:10.1029/2006GL026145.
Blewitt, G., Lavallée, D., 2002. Effect of annual signals on geodetic velocity. J. Geophys. Res. 107 (B7), 2145, doi:10.1029/2001JB000570.
Bürgmann, R., Schmidt, D., Nadeau, R.M., d'Allessio, M., Fielding, E., Manaker, D., McEvilly, T., Murray, M., 2000. Earthquake potential along the Northern Hayward Fault, California. Science 289, 1178–1182.
Cayol, V., Cornet, F.H., 1998. Effects of topography on the interpretation of the deformation field of prominent volcanoes; application to Etna. Geophys. Res. Lett. 25, 1979–1982.
Chen, Q., Freymueller, J., 2002. Geodetic evidence for a near-fault compliant zone along the San Andreas Fault in the San Francisco Bay Area. Bull. Seismol. Soc. Am. 92 (2), 656–671, doi:10.1785/0120010110.
d'Alessio, M.A., Johanson, I.A., Bürgmann, R., Schmidt, D.A., Murray, M., 2005. Slicing up the San Francisco Bay Area: block kinematics and fault slip rates from GPS-derived surface velocities. J. Geophys. Res. 110, doi:10.1029/2004JB003496.
Dietz, L., Ellsworth, W., 1990. The October 17, 1989, Loma Prieta, California, earthquake and its aftershocks: geometry of the sequence from high-resolution locations. Geophys. Res. Lett. 17 (9), 1417–1420.
Freymueller, J.T., Murray, M., Segall, P., Castillo, D., 1999. Kinematics of the Pacific-North America plate boundary zone, Northern California. J. Geophys. Res. 104, 7419–7441.
Geist, E.L., Zoback, M., 1999. Analysis of the tsunami generated by the Mw 7.8 1906 San Francisco earthquake. Geology 27 (1), 15.
Goldfinger, C., Grijalva, K., Bürgmann, R., Morey, A.E., Johnson, J.E., Hans Nelson, C., Gutiérrez-Pastor, J., Ericsson, A., Karabanov, E., Chaytor, J.D., Patton, J., Gràcia, E., 2008. Late Holocene rupture of the Northern San Andreas Fault and possible stress linkage to the Cascadia subduction zone. Bull. Seismol. Soc. Am. 98 (2), 861–889, doi:10.1785/0120060411.
Herring, T., 2005. GLOBK: Global Kalman Filter VLBI and GPS Analysis Program, Version 10.2.
Houlié, N., 2005. Mesure et Modélisation de données GPS de volcans. Applications à des études de déformation à diverses échelles et à la tomographie des panaches atmosphériques. Ph.D. Thesis, Institut de Physique du Globe de Paris.
Houlié, N., Briole, P., Puglisi, G., Bonforte, A., 2006. Large scale ground deformation of Etna observed by GPS between 1994 and 2001. Geophys. Res. Lett. 33 (2), L02309, doi:10.1029/2005GL024414.
Irwin, W., 1990. Geology and Plate-Tectonic development. The San Andreas Fault System, California, vol. 1515, pp. 61–80.
Jolivet, R., Cattin, R., Chamot-Rooke, N., Lasserre, C., Peltzer, G., 2008. Thin-plate modeling of interseismic deformation and asymmetry across the Altyn Tagh fault zone. Geophys. Res. Lett. 35 (L02309), doi:10.1029/2007GL031511.
King, N.E., Murray, M.H., Prescott, W.H., Clymer, R., Romanowicz, B., The Bay Area Regional Deformation (BARD) permanent GPS array (abstract), EOS Trans. AGU, 75(44), Fall Meeting Suppl., 470, 1994.
King, R., Bock, Y., 2006. Documentation of the GAMIT Software. MIT/SIO.
Kreemer, C., Holt, W., Haines, A., 2003. An integrated global model of present-day plate motions and plate boundary deformation. Geophys. J. Int. 154, 8–34.
Langenheim, V., Schmidt, K., Jachens, R., 1997. Coseismic deformation during the 1989 Loma Prieta earthquake and range-front thrusting along the southwestern margin of the Santa Clara Valley, California. Geology 25 (12), 1091–1094.
Le Pichon, X., Kreemer, C., Chamot-Rooke, N., 2005. Asymmetry in elastic properties and the evolution of large continental strike-slip faults. J. Geophys. Res. 110 (B03405), doi:10.1029/2004JB003343.
Lienkaemper, J., Galehouse, J., Simpson, R., 1997. Creep response of the Hayward fault to stress changes caused by the Loma Prieta earthquake 276, 2014–2016.
Lienkaemper, J., Galehouse, J., Simpson, R., 2001. Long-term monitoring of creep rate along the Hayward fault and evidence for a lasting creep response to 1989 Loma Prieta earthquake. Geophys. Res. Lett. 28 (11), 2265–2268.
Lisowski, M., Savage, J., Prescott, W., 1991. The velocity field along the San Andreas Fault in central and southern California. J. Geophys. Res. 96 (B5), 8369–8389.
Neuhauser, D., Oppenheimer, D., Zuzlewski, S., Gee, L., Murray, M., Basset, A., Prescott, W., Romanowicz, B., 2001. Collaborative projects at the Northern California Earthquake Data Center (NCEDC). Eos Trans. Am. Geophys. Union 82 (47), B563.
Pollitz, F., Nyst, M., 2005. A physical model for strain accumulation in the San Francisco Bay Region. Geophys. J. Int. 160, 302–317, doi:10.1111/j.1365-246X.2005.02433.x.
Prescott, W.H., Savage, J.C., Svarc, J.L., Manaker, D., 2001. Deformation across the Pacific-North America plate boundary near San Francisco, California. J. Geophys. Res. 106, 6673–6682, doi:10.1029/2000JB900397.
Romanowicz, B., Neuhauser, D., Bogaert, B., Oppenheimer, D., 1994. Accessing northern California earthquake data via Internet. Eos Trans. Am. Geophys. Union 75 (23), 257.
Savage, J.C., Svarc, J., Prescott, W., 1999. Geodetic estimates of fault slip rates in the San Francisco Bay Area. J. Geophys. Res. 104, 4995–5002.
Schmalzle, G., Dixon, T., Malservisi, R., Govers, R., 2006. Strain accumulation across the Carrizo segment of the San Andreas Fault California: impact of laterally varying crustal properties. J. Geophys. Res. 111 (B05403), doi:10.1029/2005JB003843.
Schön, J.H., 1996. The Physical Properties of Rocks: Fundamentals and Principles of Petrophysics, vol. 18. Pergamon, New York.
Segall, P., Lisowski, M., 1990. Surface displacement in the 1906 San Francisco and 1989 Loma Prieta earthquakes. Science 250, 1241–1243.
Sella, G.F., Dixon, A., Mao, A., 2002. A model for recent plate velocities from space geodesy. J. Geophys. Res. 107 (B4), 2081.
Thatcher, W., 1986. The crustal deformation at convergent plate margins. R. Soc. New Zealand Bull. 24, 317–332.
Thatcher, W., 1990. Present-day crustal movements and the mechanics of cylic deformation. In: The San Andreas Fault system, California, U.S. Geological Survey Professional Paper, vol. 1515, pp. 189–205.
Thurber, C., Brocher, T.M., Zhang, H., Langenheim, V., 2007. Three-dimensional P-wave velocity model for the San Francisco Bay Region, California. J. Geophys. Res. 112 (B7), 19.
Trota, A., Houlié, N., Sigmundsson, F., Jònsson, S., 2006. Deformations of the Furnas and Sete Cidade Volcanoes Velocities and further investigations. Geophys. J. Int. 166 (2), 952, doi:10.1111/j.1365-246X.2006.03039.x.
Uhrhammer, R.A., 1981. The Pacifica earthquake of 28 April 1979. Bull. Seismol. Soc. Am. 71 (4), 1161–1172.
Working Group on California Earthquake Probabilities, 2003. Earthquake Probabilities in the San Francisco Bay Region: 2002–2031 (Open File Report 03-214).